Spin-vibronic Interaction Induced Reverse Intersystem Crossing: A Case Study with TXO-TPA and TXO-PhCz Molecules

Pijush Karak,[1] Kenneth Ruud,[2, 3, a)] and Swapan Chakrabarti[1, b)]

[1)]*Department of Chemistry, University of Calcutta, 92 A. P. C. Road, Kolkata – 700009, West Bengal, India.*

[2)]*Hylleraas Centre for Quantum Molecular Sciences, Department of Chemistry, University of Tromsø – The Arctic University of Norway, 9037 Tromsø, Norway.*

[3)]*Norwegian Defence Research Establishment, P.O.Box 25, 2027 Kjeller, Norway*

(Dated: 18 December 2022)

We highlight the important roles the direct spin-orbit coupling (DSO), the spin-vibronic coupling (SV) and the dielectric constant of the medium play on the reverse intersystem crossing (RISC) mechanism of the TXO-TPA and TXO-PhCz molecules. To understand this complex phenomenon, we have calculated the RISC rate constant, k_{RISC}, using a time-dependent correlation function-based method within the framework of second-order perturbation theory. Our computed k_{RISC} in two different solvents, toluene and chloroform, suggests that in addition to the DSO, a dielectric medium-dependent SV mechanism may also have a significant impact on the net enhancement of the rate of RISC from the lowest triplet state to the first excited singlet state. Whereas we have found that k_{RISC} of TXO-TPA is mostly determined by the DSO contribution independent of the choice of solvent, the SV mechanism contributes more than 30 percent to the overall k_{RISC} of TXO-PhCz in chloroform. In toluene, however, the SV mechanism is less important for the RISC process of TXO-PhCz. An analysis of mode-specific nonadiabatic coupling (NAC) between T_2-T_1 of TXO-PhCz and TXO-TPA suggests that the NAC values in certain normal modes of TXO-PhCz are much higher than those of TXO-TPA and it is more pronounced with chloroform as a solvent. The findings demonstrate the role of the solvent-assisted SV mechanism towards the net RISC rate constant, which in turn maximizes the efficiency of thermally activated delayed fluorescence.

I. INTRODUCTION

Thermally activated delayed fluorescent (TADF) molecules without metal-organic fragments have recently seen substantial research interest because of their tantalizing prospects for use in state of the art photonics[1–10], photo-catalysis,[11] bio-imaging[12,13] and sensing,[14]. This interest has been due to the fact that conventional prompt fluorescent molecules have lower quantum efficiency than TADF molecules. After electronic excitation and subsequent fast intersystem crossing, the triplet excitons are lost either through heat dissipation to the environment or via radiative decay to the ground state, that is, phosphorescence. To improve the quantum efficiency of TADF process, the key step is the harvesting of triplet excitons vis-a-vis its transfer to an emissive singlet exciton through reverse intersystem crossing (RISC). Strong spin-orbit coupling (SOC) induced phosphorescence from T_1 to S_0 and triplet-triplet annihilation will play a detrimental role on the triplet harvesting process, making it difficult to achieve TADF. Recently, several experimental groups[15–25] have designed various types of pure organic molecules that promote triplet harvesting and the concurrent transfer of the population from the triplet state to the emissive singlet state, leading to efficient TADF processes. Additionally, many theoretical and computational works[26–34] have been presented aimed at finding design principles for developing new molecules exhibiting efficient TADF properties. Critical examination of the hitherto existing literature suggests that in addition to the locally excited (LE) states, typical pure organic TADF molecules display spatial separation of the highest occupied molecular orbital (HOMO) on the donor and the lowest unoccupied molecular orbitals (LUMO) on the acceptor moieties. This leads to strong charge-transfer (CT) character of the excited states, and these CT-type singlet- and triplet-excited states often display small energy gaps between the lowest excited singlet and triplet states, favoring the up-conversion pathway from triplet to the excited singlet state. In this context, the pioneering work of Adachi and coworkers[15,16,19,21,23,35] on metal-free organic CT molecules is worth mentioning since their discovery opened a new avenue for TADF-based third-generation light-emitting diode materials.[2,16] Ward *et al.*[24] have monitored $\Delta E_{S_1 T_1}$ and k_{RISC} constants of several molecules, which led to the conclusion that the steric effect within the D-A part plays a vital role in order to populate the S_1 state from T_1, thereby paving the way to enhance the TADF quantum yield. Furthermore, strong SOC between the first excited singlet and the triplet states is also essential because reverse intersystem crossing induced-TADF is an endothermic process. However, progress in the area of photo-dynamics has established the fact that apart from the factors mentioned above, a secondary mechanism known as spin-vibronic coupling[10,26,36–47] between S_1 and various triplet states, could increase the chance of RISC even in a situation where the energy gap between the S_1 and T_1 states ($\Delta E_{S_1 T_1}$) is large and the SOC matrix elements (SOCMEs) between these two states is vanishingly small. In principle, organic systems having donor-acceptor (DA) or donor-acceptor-donor (DAD) moieties should have very small SOC between the S_1 and T_1 states because the orbitals of the S_1 and T_1 electronic states in these systems are

a)Electronic mail: kenneth.ruud@uit.no

b)Electronic mail: swcchem@caluniv.ac.in

similar.[43,48–51] In the spin-vibronic coupling mechanism, the nonadiabatic coupling between T_1 and T_2 helps increase the population of the T_2 state and subsequent SOC-guided RISC between T_2 and S_1 leads to an efficient TADF process.

The effect of spin-vibronic interactions on k_{RISC} was first pointed out by Gibson *et al.*[40,44] It has been found[37] that spin-vibronic coupling-induced TADF efficiency is highly sensitive towards the relative position of the energy levels of the S_1, T_1 and T_2 states. The involvement of more than two triplet states in the spin-vibronic coupling-driven RISC process in certain molecules has also been proposed.[36,39,52] Moreover, careful theoretical analysis reveals that the spin-vibronic contribution to the net k_{RISC} could increase significantly on going from gas phase to the solid state.[26]

Keeping in mind the role of all these factors on the RISC mechanism, the present article is aimed at exploring the importance of the direct SOC and second-order spin-vibronic interactions in determining the net k_{RISC} of two well-known molecules, namely, TXO-TPA and TXO-PhCz. We have considered these two organic molecules due to their very high external quantum efficiency, making them good candidates[25,53] for TADF-based OLEDs and light-emitting electrochemical cells (LEC). In particular, TXO-TPA exhibits TADF-LEC properties[53] with very high luminescence efficiency. The ground-state geometries of TXO-TPA and TXO-PhCz are depicted in Fig. 1.

To understand the dynamics associated with the reverse intersystem crossing in these two systems, the time-dependent correlation function-based formalism in the framework of Fermi's Golden rule has been used for the computation of the k_{RISC} at 300K. It should be mentioned here that the correlation function-based approach have been implemented by several research groups[26,54–67] and using this formalism, nonradiative decay constants, such as internal conversion (IC), intersystem crossing (ISC) and RISC of several systems have been calculated both in the Franck-Condon and beyond Franck-Condon approximations.[57,59] Moreover, Kim *et al.*[26] have introduced the spin-vibronic coupling term to the net k_{RISC} formula through the incorporation of nonadiabatic coupling between the states concerned. They have observed that this coupling vector largely depends on the nature of the two triplet or singlet states and the energy gap between them. On the other hand, Marian *et al.*[65] and Karak *et al.*[68] have considered the spin-vibronic interaction through the explicit calculation of the derivative of the direct SOC with respect to the normal mode coordinates and successfully applied the method for calculating the rate constant of intersystem crossing. Nevertheless, in the present work, we have adopted the method developed by Kim *et al.*[26]. With our in-house developed Fortran90 code,[69] we have calculated k_{RISC} of both systems in two different solvents, namely, toluene and $CHCl_3$. The overall computational findings reveal that although k_{RISC} of TXO-TPA is almost fully determined by the direct SOC between the T_1 and S_1 states, the spin-vibronic assisted RISC proccess plays a significant role in determining the net k_{RISC} value of TXO-PhCz. These results also manifestly

reflect that spin-vibronic contribution towards the net k_{RISC} of TXO-PhCz is more prominent in $CHCl_3$ than in toluene, indicating that the solvent polarity can affect the factors determining the spin-vibronic coupling appreciably. We have considered low-polarity solvents such as toluene and chloroform because it has been found that the second-order spin-vibronic mechanism is more important in less polar solvents.[43]

The remainder of this article is organized as follows: Section II contains the theory for the calculation of k_{RISC}. In Sections III and IV, the computational details and the numerical stability of the code are discussed. Results and discussions are given in Section V. Finally, some concluding remarks are presented in Section VI.

II. THEORY

1. Theory of Reverse Intersystem Crossing Rate

Employing second-order perturbation theory in combination with Fermi's Golden rule one can express the rate constant of the RISC rate as

$$k_{RISC} = \frac{2\pi}{\hbar Z} \sum_{i,j} e^{-\beta E_{v_{bj}}} |\hat{H}'|^2 \delta(-\Delta E_{ST} + E_{v_{bj}} - E_{v_{ai}}), \quad (1)$$

where i and j represent the vibrational levels of the a-th and b-th electronic states, respectively. While ΔE_{ST} corresponds to the singlet-triplet energy gap, Z and $\hat{H}'$ denote the vibrational partition function of the initial electronic state and the Hamiltonian including spin-vibronic interaction, respectively. $\beta = \frac{1}{kT}$, where k and T are the Boltzmann constant and temperature, respectively. The Hamiltonian including spin-vibronic interaction can be written as

$$\hat{H}' = \hat{H}_{SO} + \hat{H}_{SV} \qquad (2)$$

where $\hat{H}_{SO}$ is the direct SOC operator and $\hat{H}_{SV}$ denotes the spin-vibronic (SV) interaction operator, which takes into account the non-Born-Oppenheimer contribution. In this case, we have carefully excluded the vibrational spin-orbit coupling contribution towards the net rate constant of RISC because results obtained from the previous studies reveal that the second-order spin-vibronic mechanism is particularly important when the population transfer to the S_1 state from the T_1 state is small due to the weak spin-orbit coupling between them and at the same time vibronic coupling between T_2-T_1 is strong. This means that the faster reverse internal conversion through nonadiabatic coupling between T_2 and T_1 will help transfer the population to the S_1 state from the T_2 state. A detailed discussion can be found in Ref. 43. Neglecting the direct nuclear coordinate-dependent spin-orbit coupling, the explicit inclusion of the spin-vibronic interaction can be done easily, following the approach presented in Refs. 43 and 70, and the
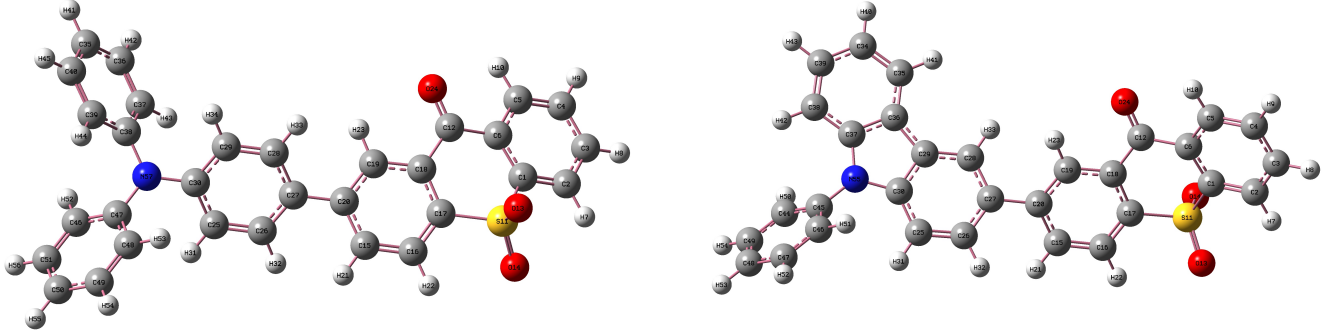
FIG. 1: The geometry of TXO-TPA (left side) and TXO-PhCz (right side).

resulting form of the matrix element of $\hat{H}'$ is given as

$$\langle S_a, v_{ai} | \hat{H}' | T_b, v_{bj} \rangle = \langle S_a, v_{ai} | \hat{H}_{SO} | T_b, v_{bj} \rangle$$

$$+ \sum_{n>b} \sum_k \frac{\langle S_a, v_{ai} | \hat{H}_{SO} | T_n, v_{nk} \rangle \langle T_n, v_{nk} | \frac{\partial}{\partial Q} | T_b, v_{bj} \rangle}{E_{T_n, v_{nk}} - E_{T_b, v_{bj}}}$$

(3)

where, S_a and T_b are the a-th singlet and b-th triplet states, respectively. The v_{ai}, v_{bj} and v_{nk} indicates the i-th, j-th and k-th vibrational level of the a-th, b-th and n-th electronic states, respectively, and $\mathbf{Q}$ is the normal mode coordinate. Furthermore, the first term in the above equation represents the direct SOC between the singlet and the triplet states while the second term corresponds to the spin-vibronic term between the triplet states coupled with the SOC between the singlet and the triplet states.

Replacing the delta function in Eq. (1) by the Fourier integral, that is,

$$\delta(-\Delta E_{ST} + E_{v_{bj}} - E_{v_{ai}}) = \frac{1}{2\pi} \int_{-\infty}^{\infty} e^{-i\Delta E_{ST} \frac{t}{\hbar}} e^{iE_{v_{bj}} \frac{t}{\hbar}} e^{-iE_{v_{ai}} \frac{t}{\hbar}} dt$$

(4)

and simultaneous substitution of Eq. (3) into Eq. (1) separates k_{RISC} into k_{RISC}^{DSO} and k_{RISC}^{SV}. We note that this separation is only valid under the Condon approximation. A simplified form of both contributions can be expressed as

$$k_{RISC}^{DSO} = \frac{|H_{SO}^{ab}|^2}{\hbar^2 Z} \int_{-\infty}^{\infty} G_{DSO}(t,t') e^{-i\Delta E_{ST} \frac{t}{\hbar}} dt,$$

(5)

where $H_{SO}^{ab} = \langle S_a, v_{ai} | \hat{H}_{SO} | T_b, v_{bj} \rangle$, and

$$k_{RISC}^{SV} = \frac{1}{\hbar^2 Z} \int_{-\infty}^{\infty} \sum_{m,m'} S'_{m,m'} G_{SV}(t,t';m,m') e^{-i\Delta E_{ST} \frac{t}{\hbar}} dt.$$

(6)

In Eq. (6), $t' = -\frac{t}{\hbar} - i\beta$ is the imaginary time and t is the real time. $S'_{m,m'}$ contains the products of the nonadiabatic coupling matrix elements and SOC term, where m and m' represents the normal modes of the initial triplet state. In Eq. (5) and Eq.

(6), $G_{DSO}(t,t')$ and $G_{SV}(t,t';m,m')$ imply the time-dependent correlation function arising from the direct SOC and spin-vibronic coupling, respectively. The detailed derivation and analysis related to these above two equations are discussed in previous work.[26,55–57,61–63,67] The complete derivation of the spin-vibronic part of the generating function ($G_{SV}(t,t';m,m')$) is also provided in the supplementary material. The explicit form of these correlation functions can be written as

$$G_{DSO}(t,t') = \sqrt{\frac{\det(\mathbf{S}_S)\det(\mathbf{S}_T)}{\det(\mathbf{W})}} exp(-\frac{i}{2\hbar}\mathbf{V}^T\mathbf{W}^{-1}\mathbf{V} + \frac{i}{\hbar}\mathbf{D}^T\mathbf{U}\mathbf{D}),$$

(7)

and

$$G_{SV}(t,t';m,m') = G_{DSO}(t,t') \times \{i\hbar \text{Tr}(\mathbf{X}\mathbf{W}^{-1}) + (\mathbf{W}^{-1}\mathbf{V})^T\mathbf{X}(\mathbf{W}^{-1}\mathbf{V}) - \mathbf{Y}^T\mathbf{W}^{-1}\mathbf{V}\},$$

(8)

where,

$$\mathbf{S}_S = \frac{\omega_S}{sin(\omega_S t)}$$

$$\mathbf{B}_S = \frac{\omega_S}{tan(\omega_S t)}$$

$$\mathbf{S}_T = \frac{\omega_T}{sin(\omega_T t'\hbar)}$$

$$\mathbf{B}_T = \frac{\omega_T}{tan(\omega_T t'\hbar)}$$

(9)

with

$$
\mathbf{X}(m,m') =
\begin{bmatrix}
0 & 0 \\
\cdot & \cdot \\
\cdot & \cdot \\
\cdot & \cdot \\
0 & 0 \\
-(\mathbf{B_S})_{m,m}(\mathbf{J^T S_T J})_{m'} & (\mathbf{B_S})_{m,m}(\mathbf{J^T B_T J})_{m'} \\
0 & 0 \\
\cdot & \cdot \\
\cdot & \cdot \\
\cdot & \cdot \\
0 & 0 \\
0 & 0 \\
\cdot & \cdot \\
\cdot & \cdot \\
\cdot & \cdot \\
0 & 0 \\
(\mathbf{S_S})_{m,m}(\mathbf{J^T S_T J})_{m'} & -(\mathbf{S_S})_{m,m}(\mathbf{J^T B_T J})_{m'} \\
0 & 0 \\
\cdot & \cdot \\
\cdot & \cdot \\
\cdot & \cdot \\
0 & 0
\end{bmatrix},
\tag{10}
$$

$$
\mathbf{W} =
\begin{bmatrix}
\mathbf{B_S} + \mathbf{J^T B_T J} & -(\mathbf{S_S} + \mathbf{J^T S_T J}) \\
-(\mathbf{S_S} + \mathbf{J^T S_T J}) & \mathbf{B_S} + \mathbf{J^T B_T J}
\end{bmatrix}
$$

$$
\mathbf{U} = (\mathbf{B_T} - \mathbf{S_T})
$$

$$
\mathbf{V} =
\begin{bmatrix}
\mathbf{J^T U D} \\
\mathbf{J^T U D}
\end{bmatrix},
\tag{11}
$$

and

$$
\mathbf{Y}(m,m') =
\begin{bmatrix}
0 \\
\cdot \\
\cdot \\
\cdot \\
0 \\
(\mathbf{B_S})_{m,m}(\mathbf{J^T U D})_{m'} \\
0 \\
\cdot \\
\cdot \\
\cdot \\
0 \\
0 \\
\cdot \\
\cdot \\
\cdot \\
0 \\
-(\mathbf{S_S})_{m,m}(\mathbf{J^T U D})_{m'} \\
0 \\
\cdot \\
\cdot \\
\cdot \\
0
\end{bmatrix}.
\tag{12}
$$

Here $\mathbf{S_T}$, $\mathbf{B_T}$, $\mathbf{S_S}$, $\mathbf{B_S}$, and $\mathbf{U}$ are all N×N diagonal matrices, and the subscripts S and T refer to the singlet (S_1) and triplet (T_1) states, respectively. $\mathbf{W}$ and $\mathbf{X}$ are 2N×2N matrices whereas $\mathbf{Y}$ and $\mathbf{V}$ are 2N×1 column vectors. The m-th row of the $\mathbf{X}$ matrix in Eq. (10) is denoted as $\pm(\mathbf{B_S}\backslash\mathbf{S_S})_m(\mathbf{J^T}(\mathbf{S_T}\backslash\mathbf{B_T})\mathbf{J})_{m'}$ which follows from the multiplication of the m'th row of $(\mathbf{J^T}(\mathbf{S_T}\backslash\mathbf{B_T})\mathbf{J})_{m'}$ matrix by $(\mathbf{B_S}\backslash\mathbf{S_S})_{m,m}$. The same notation is used in the formation of the $\mathbf{Y}$ vector as written in Eq. (12). The frequencies of the singlet (S_1) and triplet (T_1) states are given by ω_S and ω_T, respectively. It should be noted that the normal mode coordinates of the singlet and triplet states are connected by the following relation,

$$
\mathbf{Q_T} = \mathbf{J Q_S} + \mathbf{D},
\tag{13}
$$

where $\mathbf{J}$ is the Duschinsky rotation matrix connecting these two states through the displacement vector, $\mathbf{D}$, and the transpose of $\mathbf{J}$ in all the above equations is denoted by $\mathbf{J^T}$.

Using these equations, the total k_{RISC} rate can be expressed as

$$
k_{RISC}^{total} = k_{RISC}^{DSO} + k_{RISC}^{SV}
$$

$$
= \frac{1}{\hbar^2 Z} \int_{-\infty}^{+\infty} \left(|H_{SO}^{ab}|^2 G_{DSO}(t,t') + \sum_{m,m'} S'_{m,m'} G_{SV}(t,t';m,m') \right)
$$

$$
e^{-i\Delta E_{ST}\frac{t}{\hbar}} dt
\tag{14}
$$

III. DISCUSSIONS ABOUT THE CODE DEVELOPMENT

Our developed Fortran90 code[69] evaluates the correlation function for both the direct SOC and SV part in the time domain and involves complex matrix multiplication, inverse and determinant calculations. The most difficult part of Eq. (14) is the evaluation of the correlation function for the spin-vibronic term, where it is necessary to evaluate $G_{SV}(t,t';m,m')$ for each pair of normal mode frequencies (m,m') at every time step. In particular, the calculation of $G_{SV}(t,t';m,m')$ for 20000 time steps on a single core requires almost 27.7 days for a system having 165 normal modes and this could be achieved by efficient parallelization of the code given that the correlation functions at different times intervals are independent of each other. In the present context, we have implemented MPI parallelization only for the part of the code that computes $G_{SV}(t,t';m,m')$. We have used 120 cores from 4 computing nodes and calculated $G_{SV}(t,t';m,m')$ for both TXO-TPA and TXO-PhCz molecules having 165 and 159 normal modes, respectively. The wall times are reduced to 15.5 hrs and 13 hrs, for TXO-TPA and TXO-PhCz, respectively. The time-dependent correlation functions are evaluated for 20000 grid points in the time interval ranging from -10ps to +10ps. Since we are interested in probing the effect of the spin-vibronic coupling on the rate constant of RISC for the individual normal modes, we have transformed the generating function at each time step to the frequency domain. The transformations have been carried out using the FFTW3 package.[71] The use of a Lorentzian damping function with a small damping parameter of 50 cm^{-1} further ensures the decay of the correlation function within a very short timescale (fs).

TABLE I: Energy gap, spin-orbit coupling matrix element (SOCME) and norm of the nonadiabatic coupling vector (NACV) of both TXO-TPA and TXO-PhCz in toluene as well as CHCl$_3$ solvents.

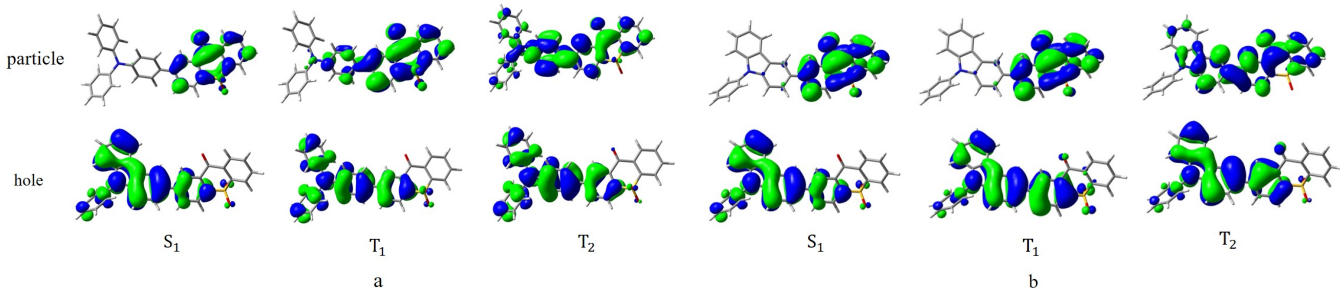| System	Solvent	$\Delta E_{S_1-T_1}$ (eV)	SOCME$_{S_1-T_1}$ (cm^{-1})	SOCME$_{S_1-T_2}$ (cm^{-1})	$\Delta E_{T_1-T_2}$ (eV)	NAC$_{T_2-T_1}$ (bohr^{-1})
TXO-TPA	touene	0.11	0.072	0.38	0.73	3.83
	CHCl$_3$	0.13	0.076	0.35	0.76	3.76
TXO-PhCz	toluene	0.21	0.15	0.81	0.69	5.09
	CHCl$_3$	0.21	0.13	0.69	0.73	8.47

FIG. 2: The hole-particle states of (a) TXO-TPA and (b) TXO-PhCz in toluene solvent.

IV. GEOMETRY AND COMPUTATIONAL PERSPECTIVE

The ground state (S$_0$) and all other excited (S$_1$, T$_1$ and T$_2$) states of both TXO-TPA and TXO-PhCz were optimized using the 6-311G(d,p) basis in combination with the M06[72] hybrid functional. The optimizations were carried out with toluene and CHCl$_3$ as implicit solvents and for this purpose, we have used the polarizable continuum model (PCM)[73] as implemented in Gaussian16.[74] The computation of the normal-mode frequencies has been done within the harmonic approximation, which has certain limitations in capturing the vibrational effects of through-space or long-range charge-transfer systems. In order to check the suitability of the selected exchange–correlation functionals, one more functional, namely, PBE0[75] has also been considered, and the relevant results are provided in the supplementary material. Interestingly, range-separated exchange-correlation functionals such as CAM-B3LYP[76] and ωB97XD,[77] fail to capture the correct geometry of the T$_2$ state of both TXO-TPA and TXO-PhCz and as a result, restricting the choice of functionals that can be used in geometry optimizations.

The calculations of mode-specific nonadiabatic coupling matrix elements (NACMEs) between T$_2$ and T$_1$ is not straightforward, and in the mode-specific representation, the NACMEs between T$_2$ and T$_1$ can be expressed as

$$\langle T_2|\frac{\partial}{\partial Q_k}|T_1\rangle = \frac{\langle T_2|\frac{\partial V}{\partial Q_k}|T_1\rangle}{E_{T_2} - E_{T_1}} \qquad (15)$$

where, $\hat{V}$ is the electron-nucleus attraction operator and $\mathbf{Q}_k$ represents the normal coordinate of the k-th mode. $E_{T_2} - E_{T_1}$ denotes the energy gap between the T$_2$ and T$_1$ states. To extract the NACMEs between the T$_2$ and T$_1$ states, we have used solvent-optimized T$_2$ geometries of both molecules and

the computations have been performed using the OpenMolcas software[78,79]. The basis set chosen is 6-311G** and the active space used CASSCF (6e/10o). After getting the Cartesian components of the non-adiabatic coupling vectors, we have transformed it to the normal coordinate representation as shown in Eq. (16).

$$\langle T_2|\frac{\partial}{\partial Q_k}|T_1\rangle = \sum_i \sum_j L_{ij}^T \langle T_2|\frac{\partial}{\partial q_{ij}}|T_1\rangle \frac{1}{\sqrt{M_i}} \qquad (16)$$

Here, i is the atomic index and j denotes the Cartesian components (x, y and z) of an atom in a particular normal mode, k. L is the eigenvector matrix of the mass-weighted Hessian in Cartesian representation and q and M indices are the Cartesian coordinates and mass of the nuclei, respectively. ORCA 5.0.2[80,81] has been used to compute the SOC matrix elements and the energy gap (ΔE) and the calculations have been performed with the M06 exchange–correlation functional and the def2-TZVP basis at the TDDFT level of theory. The use of def2/JK as auxiliary basis with the RI-JK approximation helped reduce the overall computational cost. Different levels of theory have been used for the computation of SOCMEs and NACMEs. Previous theoretical studies[82] have shown that both TDDFT and wave function-based methods give results of comparable accuracy for molecules having SOCMEs smaller than 1 cm^{-1} and the data in Table I indicate that the choice of method would hardly affect the SOCME values of the studied systems. In addition, the computation of NACMEs at the level of TDDFT was found to be consistent with the corresponding outcome of various multireference approaches[83,84] except in the case of conical intersections, where the multireference techniques are more reliable than TDDFT based methods.[85] Neither TDDFT nor CASSCF will in general be able to provide quantitative agreement with experiment. Given their similar performance

for the calculation SOCMEs and NACMEs, we believe the accuracy of our results for the rate constant of RISC is comparable that which would be achieved if TDDFT could be used for all calculations.

V. RESULTS AND DISCUSSIONS

It is well known that efficient ISC between S_1 and T_1 is a prerequisite condition to achieve thermally activated delayed fluorescence through the RISC process. The experimental values of k_{ISC} for TXO-TPA and TXO-PhCz are found to be $3.79 \times 10^7 s^{-1}$ and $5.15 \times 10^7 s^{-1}$, respectively. To benchmark these experimental findings, we have computed the k_{ISC} for both systems using our previously developed code 68. The corresponding k_{ISC} data both in gas phase and in the studied solvents are collected in Table SIV of the supplementary material. The theoretical k_{ISC} values for TXO-TPA and TXO-PhCz in the $S_1 \rightarrow T_1$ channel are found to be of the order of $10^7 s^{-1}$, in good agreement with the experimental findings of Refs.25, 53, and 86.

As mentioned earlier, small $\Delta E_{S_1 T_1}$ and strong SOC between S_1 and T_1 are the two most important criteria to be satisfied to ensure noticeable RISC processes in molecules exhibiting TADF at room temperature. The computed $\Delta E_{S_1 T_1}$ and SOCMEs at the TDDFT level of theory suggest that $\Delta E_{S_1 T_1}$ of TXO-TPA in toluene and CHCl$_3$ are 0.11 eV and 0.13 eV, respectively, while the corresponding energy gap for TXO-PhCz is 0.21 eV and, as evident from Table I, this value is independent of the nature of the solvent used. Usually molecules having $\Delta E_{S_1 T_1}$ around 0.2 eV are good candidates for TADF and looking at the $\Delta E_{S_1 T_1}$ values for both systems, it seems reasonable that both of them satisfies this criterion.[1,6,25] The computed energy gaps ($\Delta E_{S_1 T_1}$ and $\Delta E_{S_1 T_2}$) and the SOCMEs (SOCME$_{S_1 T_1}$ and SOCME$_{S_1 T_2}$) of these two molecules in gas phase are also collected in Table SIII of the supplementary material. Table I also reveals that SOCME between S_1 and T_1 of TXO-TPA is negligibly small while that of TXO-PhCz is marginally higher and this is true irrespective of the nature of the solvent. The small SOCME between S_1 and T_1 in both systems is not surprising given that the nature of the hole and particle states of the S_1 and T_1 states of the two systems are of charge transfer (CT) type. More precisely, the S_1 and T_1 states of TXO-TPA have ^{1}CT-^{3}CT character which prohibits large SOCME as guided by the El-Sayed's rule.[87] In contrast, Table I shows that the SOCME between S_1 and T_2 is higher than that of S_1 and T_1 because the T_2 state of TXO-TPA exhibits both local excitation (^{3}LE) and ^{3}CT character and this leads to partial relaxation of El-Sayed's rule. The relevant hole and particle states of the S_1, T_1 and T_2 states of TXO-TPA in toluene are depicted in Fig. 2. However, the T_2 state of both systems lies above the S_1 state and as a consequence, the chance of uphill ISC-guided RISC is small. At this point, it is worth recalling that the higher-lying T_n states also can participate in the RISC process through the spin-vibronic mechanism.

The values of the SOCMEs between S_1 and T_1 and S_1 and T_2 of TXO-PhCz also follow similar trend as that of TXO-TPA. Also in this case the T_2 state has ^{3}LE+^{3}CT character while the ^{1}CT$-^3$CT character is consistent for the S_1 and T_1 states as is evident from Fig. 2. The hole and particle states of both systems in chloroform are presented in the supplementary material.

The experimental results[24,25,53] suggest that both TXO-TPA

TABLE II: Direct spin-orbit coupling (DSO) and spin-vibronic (SV) aided k_{RISC} of the $T_1 \rightarrow S_1$ pathway.

System	Medium	k_{RISC}^{DSO} (s^{-1})	k_{RISC}^{SV} (s^{-1})
TXO-TPA	toluene	2.14×10^4	1.59×10^3
	CHCl$_3$	2.17×10^4	0.92×10^3
TXO-PhCz	toluene	3.87×10^4	0.84×10^4
	CHCl$_3$	3.60×10^4	1.69×10^4

TABLE III: Percentage of contribution of DSO and SV mechanisms to the RISC rate constant.

System	Solvent	$\%k_{RISC}^{DSO}$	$\%k_{RISC}^{SV}$
TXO-TPA	touene	93.08	6.92
	CHCl$_3$	95.92	4.08
TXO-PhCz	toluene	82.07	17.93
	CHCl$_3$	68.05	31.95

and TXO-PhCz in the form of solid films will have k_{RISC} values of the order of 10^4 s^{-1}. In a more recent work[86] on TXO-TPA, the corresponding experimental k_{RISC} value has been found to be 2.28×10^5 s^{-1} which suggests that the host material used for the preparation of the thin film affects the value of k_{RISC} of TXO-TPA. At the theoretical level, we first aimed at calculating k_{RISC}^{DSO} using Eq. (14), which means that we need to compute the correlation function ($G_{DSO}(t,t')$) for the direct SOC interaction. For this purpose, in addition to $\Delta E_{S_1 T_1}$, the Duschinsky rotation matrix (**J**), displacement vectors (**D**) and frequencies of the S_1 and T_1 states are used as input to our code. Eq. (14) further demonstrates that the Fourier transformation can help us extract the correlation function as a function of the lowest excited singlet-triplet energy gap ($\Delta E_{S_1 T_1}$). After getting the Fourier transformed $G_{DSO}(t,t')$ and multiplying it with the square of the SOCMEs, we obtain k_{RISC}^{DSO} as a function of $\Delta E_{S_1 T_1}$. The variation of k_{RISC}^{DSO} with respect to $\Delta E_{S_1 T_1}$ for both systems in toluene and chloroform are shown in Fig. 3 and the correct k_{RISC}^{DSO} values of the systems are then extracted by placing vertical dotted black lines at system-specific $\Delta E_{S_1 T_1}$ values as given in Table I. These figures will aid the reader in understanding how the RISC rate constant is calculated in the frequency domain. The k_{RISC}^{DSO} values of TXO-TPA and TXO-PhCz in toluene and chloroform are collected in Table II. The corresponding k_{ISC} and k_{RISC} values in gas phase has also been provided in Table SIV of the supplementary material. From Table II, it is evident that the value k_{RISC}^{DSO} of TXO-TPA in toluene is 2.14×10^4 s^{-1} and that in chloroform is 2.17×10^4 s^{-1},
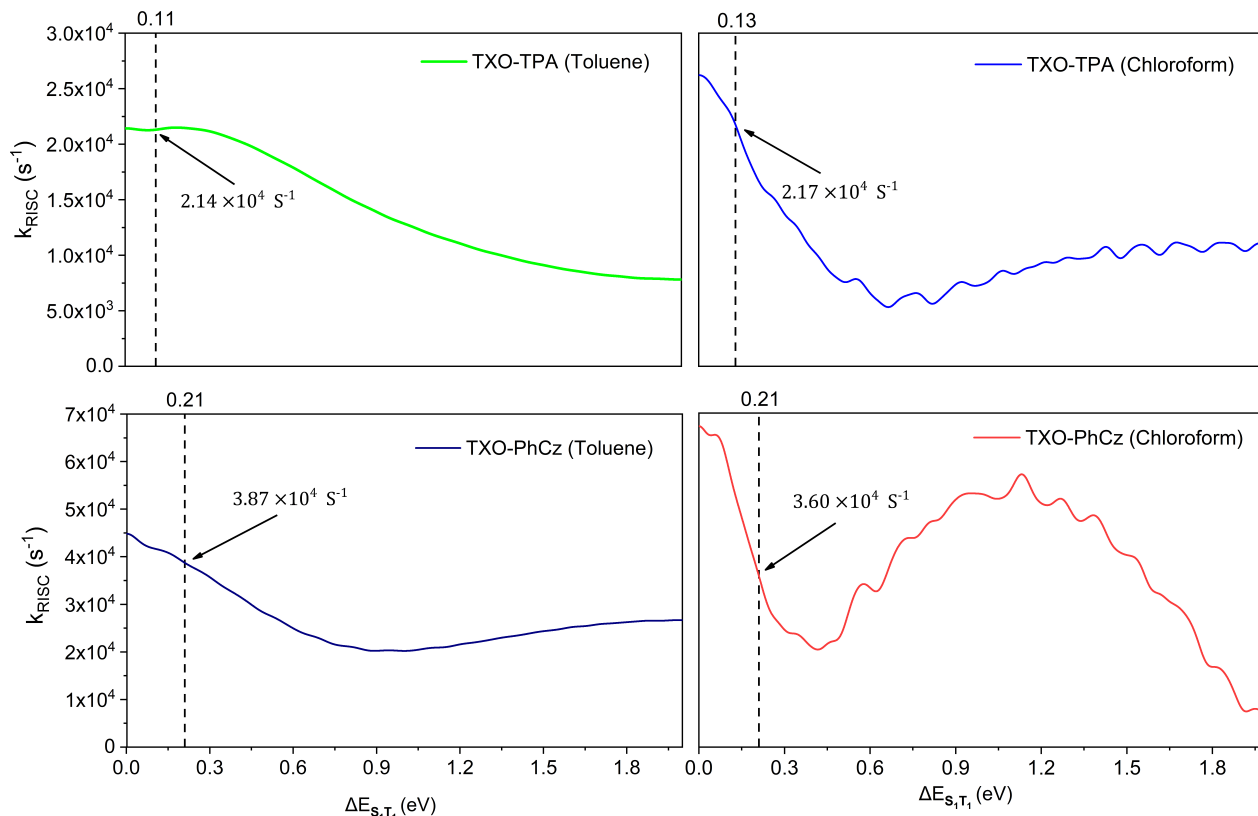
FIG. 3: Nature of variation of the DSO induced RISC rate constant of TXO-TPA and TXO-PhCz in toluene and CHCl$_3$ dielectric solvents with respect to the energy gap. The black dotted vertical line indicates the rate constant calculated at a particular singlet-triplet energy gap.

indicating that solvent polarity has no impact on k_{RISC}^{DSO} of TXO-TPA. The present theoretically evaluated k_{RISC} value of TXO-TPA is notably smaller than the theoretical k_{RISC} value given in Ref. 86. This discrepancy is due to Gillett *et al.*[86] taking a conservative estimate for SOCME of 0.5 cm^{-1} after considering several geometries along the triplet trajectories that evolve in the presence of explicit toluene solvent molecules. Because the excited singlet state has a certain lifetime, we prefer to compute the SOCME on the S$_1$ optimized geometry. Nonetheless, our calculations reveal that the SOCME between S$_1$ and T$_1$ using the excited triplet state geometry will be 0.24 cm^{-1} and the corresponding k_{RISC} for TXO-TPA will reach 1.53×10^5 s^{-1}. We note that k_{RISC}^{DSO} of TXO-PhCz also does not have any solvent dependency and the corresponding values of k_{RISC}^{DSO} are 3.87×10^4 s^{-1} and 3.60×10^4 s^{-1} in toluene and chloroform, respectively. This finding is quite consistent with the results presented in Table I, which clearly shows that neither $\Delta E_{S_1T_1}$ nor SOCME have any significant solvent dependence. Table II also illustrates that k_{RISC}^{DSO} of TXO-PhCZ in both solvents is slightly higher than that of TXO-TPA albeit a closer inspection of

the SOCMEs of both systems, as given Table I, suggests that an approximately four times higher value of k_{RISC}^{DSO} of TXO-PhCZ was to be expected since SOCME appears in the rate expression as a square term. However, an approximately two times higher $\Delta E_{S_1T_1}$ of TXO-PhCz over TXO-TPA keeps the value of k_{RISC}^{DSO} of TXO-PhCz lower than expected.

With this background, we now try to decipher the role of spin-vibronic coupling on the rate of RISC of TXO-TPA and TXO-PhCz. In general, it is expected that the spin-vibronic contribution will become important when the SOCME between S$_1$ and T$_1$ is small and normal mode-specific NACME between T$_1$ and T$_2$ is large. Higher-lying T$_n$ states can also participate in the spin-vibronic mechanism but the chance of such a process occurring is rather small. In this case too, the calculation of k_{RISC}^{SV} proceeds through the evaluation of the spin-vibronic correlation function following Eq. (6). In addition, $S'(m,m')$ also needs to be calculated before performing the FFT. Apart from using $\Delta E_{S_1T_1}$ and SOCMEs (S$_1$-T$_2$) from Table I, the computation of $S'(m,m')$ has been carried out by employing normal mode-specific NACMEs between T$_2$ and
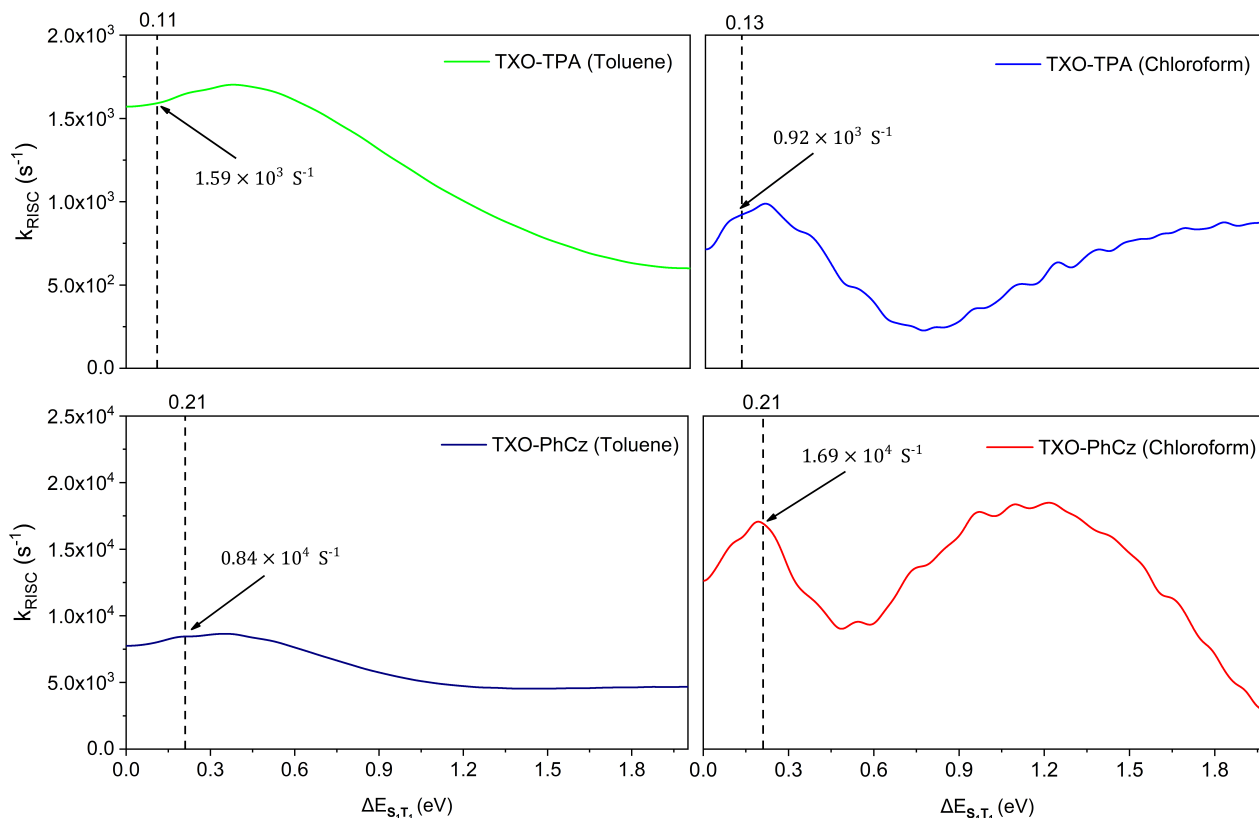
FIG. 4: Variation of the RISC rate constant with $\Delta E_{S_1 T_1}$ of TXO-TPA and TXO-PhCz for the spin-vibronic interaction in both toluene and CHCl$_3$ solvents. The black dotted vertical line indicates the rate constant calculated at a particular singlet-triplet energy gap.

T_1 and the energy gap between these two triplet states, and finally k_{RISC}^{SV} has been evaluated with respect to $\Delta E_{S_1 T_1}$ following the same method as done before. The variation of k_{RISC}^{SV} as a function of $\Delta E_{S_1 T_1}$ for both molecules is shown in Fig. 4. The mode-specific NACMEs of both molecules are provided in the supplementary material.

The values of k_{RISC}^{SV} of TXO-TPA and TXO-PhCz in toluene and chloroform are given Table II. In the case of TXO-TPA, k_{RISC}^{SV} values are found to be 1.59×10^3 s^{-1} and 0.92×10^3 s^{-1} in toluene and chloroform, respectively. The corresponding values for TXO-PhCz in toluene and chloroform are 0.84×10^4 s^{-1} and 1.69×10^4 s^{-1}, respectively. These findings indicate that the dominant contribution to the overall k_{RISC} comes from the direct SOC between S_1 and T_1 and in particular that spin-vibronic coupling has no influence on the net k_{RISC} of TXO-TPA in neither of the solvents. The detailed results are provided in Table III and shows that spin-vibronic coupling contributes only 6.92% and 4.08% to the net k_{RISC} of TXO-TPA in toluene and chloroform, respectively. However, spin-vibronic coupling plays a substantial role in determining the net k_{RISC} of the

TXO-PhCz molecule, and remarkably the SV contribution may go up to 31.95% in chloroform.

From Eq. (3), it is easy to understand that three factors, $SOC_{S_1-T_2}$, $\Delta E_{T_2-T_1}$ and NACMEs between T_2 and T_1 will control the strength of the SV mechanism in the RISC process and the corresponding values of the first two factors along with the norm of the nonadiabatic coupling vector for TXO-TPA and TXO-PhCz molecules in both solvents can be found in Table I. It is clear from Table I that albeit no significant difference in the values of $SOC_{S_1-T_2}$ and $\Delta E_{T_2-T_1}$ are observed for TXO-TPA and TXO-PhCz in either of the solvents, a comparison of the norm of the nonadiabatic coupling vector between T_2 and T_1 of the two systems indicates that normal mode-specific NACMEs could be the key factor in driving strong spin-vibronic coupling induced RISC in TXO-PhCz compared to TXO-TPA. The method of calculating the normal mode-specific NACMEs is discussed in the computational details section and the magnitude of the mode-specific NACMEs for all the normal modes of TXO-TPA and TX0-PhCz in both solvents are shown in
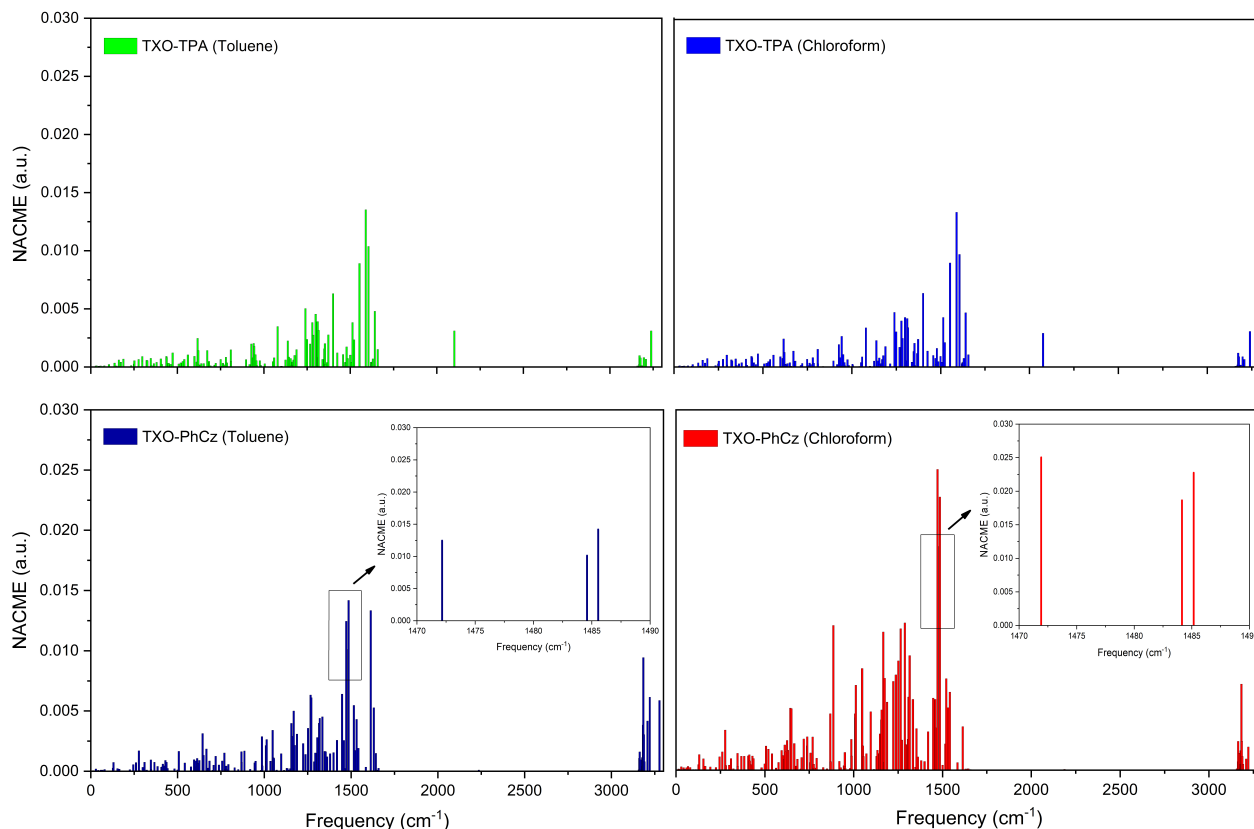
FIG. 5: Mode specific nonadiabatic coupling matrix elements (NACMEs) between the T_2 and T_1 of TXO-TPA and TXO-PhCz in toluene as well as chloroform solvents computed at the optimized T_2 geometry. The insets indicate the NACMEs in the frequency range of 1470-1490 cm^{-1}.

Fig. 5. It is to be noted that the number of normal modes of TXO-TPA is 165 while that of TXO-PhCz is 159. It is readily perceived from Fig. 5. that the dominant NACME between T_2 and T_1 comes from specific normal modes, in both molecules centered around 1500 cm^{-1}. More precisely, NACMEs between T_2 and T_1 of TXO-TPA is relatively higher in three normal modes having frequencies 1552 cm^{-1}, 1589 cm^{-1} and 1604 cm^{-1}, and solvent polarity hardly has any impact on these values. In contrast, three major NACMEs are identified at frequencies 1472 cm^{-1}, 1485 cm^{-1} and 1613 cm^{-1} for TXO-PhCz in toluene and this result changes quite a bit in chloroform where three intense peaks have appeared in the frequency range 1470 cm^{-1} to 1490 cm^{-1}. These peaks are very closely spaced with respect to one another and hence to have a better visualization of these three normal mode-specific NACMEs, we have plotted them as depicted in the inset of Fig. 5. This makes a huge difference in the spin-vibronic coupling mechanism of TXO-TPA and TXO-PhCz. Moreover, several other prominent peaks are also found in between 885 cm^{-1} and 1287 cm^{-1} for TXO-PhCz in chloroform. The important normal modes of both TXO-TPA and TXO-PhCz in toluene and chloroform are presented in the supplementary material.

To describe the effect of the spin-vibronic mechanism quantitatively, k_{RISC}^{SV} values for a few selected normal modes with relatively high NACMEs of both the systems in toluene and chloroform are computed independently, and the relevant results are collected in Table IV. We see that even considering normal modes having relatively high NACMEs, k_{RISC}^{SV} of TXO-TPA never reaches the order (10^4 s^{-1}) of k_{RISC}^{DSO}, indicating that RISC in TXO-TPA occurs only via the direct SOC pathway ($T_1 \rightarrow S_1$). Table IV also suggests that k_{RISC}^{SV} of TXO-PhCz is ten times higher than that of TXO-TPA and considering all the contributing normal modes with large NACMEs in chloroform, the resultant k_{RISC}^{SV} value attains the same order of magnitude (10^4 s^{-1}) as that of k_{RISC}^{DSO}, which suggests that the spin-vibronic mechanism will have profound impact on the RISC process of TXO-PhCz in chloroform.

VI. CONCLUSIONS

To summarize, we have demonstrated the explicit role of direct spin-orbit coupling (DSO) and spin-vibronic (SV) interaction on the reverse intersystem crossing process in a pair of thermally activated delayed fluorescent molecules, namely, TXO-TPA and TXO-PhCz. To compute k_{RISC} of both sys-

TABLE IV: Mode specific RISC rate constants.

System	Solvent	mode number	Frequency (cm^{-1})	k_{RISC}^{SV} (s^{-1})
TXO-TPA	Toluene	ω_{135}	1552.81	1.95×10^2
		ω_{136}	1589.19	4.45×10^2
		ω_{137}	1604.78	2.71×10^2
TXO-TPA	CHCl$_3$	ω_{135}	1552.58	1.17×10^2
		ω_{136}	1588.95	2.66×10^2
		ω_{137}	1605.51	1.38×10^2
TXO-PhCz	Toluene	ω_{124}	1472.16	0.89×10^3
		ω_{126}	1485.54	1.16×10^3
		ω_{134}	1613.85	1.13×10^3
		ω_{154}	3183.73	0.96×10^3
TXO-PhCz	CHCl$_3$	ω_{72}	885.76	0.52×10^3
		ω_{100}	1166.39	0.60×10^3
		ω_{106}	1250.96	0.40×10^3
		ω_{107}	1264.24	0.69×10^3
		ω_{109}	1287.83	0.75×10^3
		ω_{124}	1471.91	3.61×10^3
		ω_{125}	1484.14	1.99×10^3
		ω_{126}	1485.16	2.96×10^3

tems, the time-dependent correlation functions that include DSO and SV contributions separately are evaluated in toluene and chloroform. The results suggest that the RISC process in TXO-TPA is mostly determined by the DSO and solvent polarity neither facilitates the RISC rate nor changes the mechanism involved in the RISC process. However, careful examination of k$_{RISC}$ values of TXO-PhCz reveals that although the RISC process in this molecule is mainly governed by DSO, SV also contributes substantially to the overall rate constant of TXO-PhCz. Moreover, in this case the SV interaction is strongly dependent on the solvent polarity. To get insight into the origin of this interesting phenomenon, we have calculated the normal mode-specific k$_{RISC}^{SV}$ and found that very strong nonadiabatic coupling between T$_2$ and T$_1$ in selected normal modes of TXO-PhCz in chloroform is responsible for more than 30 percent of the SV contribution to the net k$_{RISC}$ in this molecule. In brief, the present work emphasizes the importance of solvent polarity-assisted spin-vibronic mechanism in the RISC process.

SUPPLEMENTARY MATERIAL

Supplementary material contains the Cartesian coordinates of TXO-TPA and TXO-PhCz in the gas and solvent phase, complete derivation of the spin-vibronic part of the correlation function, choice of the functionals for geometry optimization, emission wavelengths, normal mode frequencies of TXO-TPA and TXO-PhCz, gas phase data, k$_{ISC}$ for both the molecules in the gas and solvent phases, mode specific k$_{RISC}$ in solvent phase, k$_{RISC}$ data in gas phase, natural transition orbitals of both the systems in chloroform, displacement vectors and Duschinsky rotation matrices.

AUTHOR DECLARATIONS

Conflict of Interest

The authors have no conflicts to disclose.

DATA AVAILABILITY

The data that supports the findings of this study are available within the article [and its supplementary material].

[1] A. Endo, K. Sato, K. Yoshimura, T. Kai, A. Kawada, H. Miyazaki, and C. Adachi, Appl. Phys. Lett. **98**, 083302 (2011).
[2] C. Adachi, Jpn. J. Appl. Phys. **53**, 060101 (2014).
[3] Y. Wada, H. Nakagawa, S. Matsumoto, Y. Wakisaka, and H. Kaji, Nat. Photon. **14**, 643 (2020).
[4] D. H. Ahn, S. W. Kim, H. Lee, I. J. Ko, D. Karthik, J. Y. Lee, and J. H. Kwon, Nat. Photon. **13**, 540 (2019).
[5] K. Goushi, K. Yoshida, K. Sato, and C. Adachi, Nat. Photon. **6**, 253 (2012).
[6] Z. Yang, Z. Mao, Z. Xie, Y. Zhang, S. Liu, J. Zhao, J. Xu, Z. Chi, and M. P. Aldred, Chem. Soc. Rev. **46**, 915 (2017).

[7] Y. Liu, C. Li, Z. Ren, S. Yan, and M. R. Bryce, Nat. Rev. Mater. **3**, 18020 (2018).

[8] X.-K. Chen, D. Kim, and J.-L. Brédas, Acc. Chem. Res. **51**, 2215 (2018).

[9] J. Eng and T. J. Penfold, Commun. Chem. **4**, 91 (2021).

[10] T. J. Penfold, F. B. Dias, and A. P. Monkman, Chem. Commun. **54**, 3926 (2018).

[11] E. Speckmeier, T. G. Fischer, and K. Zeitler, J. Am. Chem. Soc. **140**, 15353 (2018).

[12] X. Xiong, F. Song, J. Wang, Y. Zhang, Y. Xue, L. Sun, N. Jiang, P. Gao, L. Tian, and X. Peng, J. Am. Chem. Soc. **136**, 9590 (2014).

[13] T. Li, D. Yang, L. Zhai, S. Wang, B. Zhao, N. Fu, L. Wang, Y. Tao, and W. Huang, Adv. Sci. **4**, 1600166 (2017).

[14] F. Ni, N. Li, L. Zhan, and C. Yang, Adv. Opt. Mater. **8**, 1902187 (2020).

[15] S. Hirata, Y. Sakai, K. Masui, H. Tanaka, S. Y. Lee, H. Nomura, N. Naka-mura, M. Yasumatsu, H. Nakanotani, Q. Zhang, K. Shizu, H. Miyazaki, and C. Adachi, Nat. Mater. **14**, 330 (2015).

[16] H. Uoyama, K. Goushi, K. Shizu, H. Nomura, and C. Adachi, Nature **492**, 234 (2012).

[17] Q. Zhang, J. Li, K. Shizu, S. Huang, S. Hirata, H. Miyazaki, and C. Adachi, J. Am. Chem. Soc. **134**, 14706 (2012).

[18] F. B. Dias, K. N. Bourdakos, V. Jankus, K. C. Moss, K. T. Kamtekar, V. Bhalla, J. Santos, M. R. Bryce, and A. P. Monkman, Adv. Mater. **25**, 3707 (2013).

[19] L.-S. Cui, H. Nomura, Y. Geng, J. U. Kim, H. Nakanotani, and C. Adachi, Angew. Chem. Int. Ed. **56**, 1571 (2017).

[20] B. Huang, W. Chen, and Z. Li, Angew. Chem. Int. Ed. **57**, 12473 (2018).

[21] M. Inoue, T. Serevičius, H. Nakanotani, K. Yoshida, T. Matsushima, S. Juršėnas, and C. Adachi, Chem. Phys. Lett. **644**, 62 (2016).

[22] F. B. Dias, K. N. Bourdakos, V. Jankus, K. C. Moss, K. T. Kamtekar, V. Bhalla, J. Santos, M. R. Bryce, and A. P. Monkman, Adv. Mater. **25**, 3707 (2013).

[23] H. Nakanotani, T. Higuchi, T. Furukawa, K. Masui, K. Morimoto, M. Nu-mata, H. Tanaka, Y. Sagara, T. Yasuda, and C. Adachi, Nat. Commun. **5**, 4016 (2014).

[24] J. S. Ward, R. S. Nobuyasu, A. S. Batsanov, P. Data, A. P. Monkman, F. B. Dias, and M. R. Bryce, Chem. Commun. **52**, 2612 (2016).

[25] H. Wang, L. Xie, Q. Peng, L. Meng, Y. Wang, Y. Yi, and P. Wang, Adv. Mater. **26**, 5198 (2014).

[26] I. Kim, S. O. Jeon, D. Jeong, H. Choi, W.-J. Son, D. Kim, Y. M. Rhee, and H. S. Lee, J. Chem. Theory Comput. **16**, 621 (2020).

[27] T. J. Penfold, J. Phys. Chem. C **119**, 13535 (2015).

[28] P. K. Samanta, D. Kim, V. Coropceanu, and J.-L. Brédas, J. Am. Chem. Soc. **139**, 4042 (2017).

[29] N. Aizawa, Y. Harabuchi, S. Maeda, and Y.-J. Pu, Nat. Commun. **11**, 3909 (2020).

[30] A. Pershin, D. Hall, V. Lemaur, J.-C. Sancho-Garcia, L. Muccioli, E. Zysman-Colman, D. Beljonne, and Y. Olivier, Nat. Commun. **10**, 597 (2019).

[31] Y. Olivier, M. Moral, L. Muccioli, and J.-C. Sancho-García, J. Mater. Chem. C **5**, 5718 (2017).

[32] K. Liang, C. Zheng, K. Wang, W. Liu, Z. Guo, Y. Li, and X. Zhang, Phys. Chem. Chem. Phys. **18**, 26623 (2016).

[33] Y. Olivier, J.-C. Sancho-Garcia, L. Muccioli, G. D'Avino, and D. Beljonne, J. Phys. Chem. Lett. **9**, 6149 (2018).

[34] H. Sun, Z. Hu, C. Zhong, X. Chen, Z. Sun, and J.-L. Brédas, J. Phys. Chem. Lett. **8**, 2393 (2017).

[35] J. U. Kim, I. S. Park, C.-Y. Chan, M. Tanaka, Y. Tsuchiya, H. Nakanotani, and C. Adachi, Nat. Commun. **11**, 1765 (2020).

[36] I. Kim, K. H. Cho, S. O. Jeon, W.-J. Son, D. Kim, Y. M. Rhee, I. Jang, H. Choi, and D. S. Kim, JACS Au **1**, 987 (2021).

[37] M. K. Etherington, J. Gibson, H. F. Higginbotham, T. J. Penfold, and A. P. Monkman, Nat. Commun. **7**, 13680 (2016).

[38] M. K. Etherington, F. Franchello, J. Gibson, T. Northey, J. Santos, J. S. Ward, H. F. Higginbotham, P. Data, A. Kurowska, P. L. Dos Santos, D. R. Graves, A. S. Batsanov, F. B. Dias, M. R. Bryce, T. J. Penfold, and A. P. Monkman, Nat. Commun. **8**, 14987 (2017).

[39] I. Lyskov and C. M. Marian, J. Phys. Chem. C **121**, 21145 (2017).

[40] J. Gibson, A. P. Monkman, and T. J. Penfold, Chem .Phys. Chem. **17**, 2956 (2016).

[41] X.-K. Chen, S.-F. Zhang, J.-X. Fan, and A.-M. Ren, J. Phys. Chem. C **119**, 9728 (2015).

[42] T. Northey and T. Penfold, Org. Electron. **59**, 45 (2018).

[43] T. J. Penfold, E. Gindensperger, C. Daniel, and C. M. Marian, Chem. Rev. **118**, 6975 (2018).

[44] J. Gibson and T. J. Penfold, Phys. Chem. Chem. Phys. **19**, 8428 (2017).

[45] E. W. Evans, Y. Olivier, Y. Puttisong, W. K. Myers, T. J. H. Hele, S. M. Menke, T. H. Thomas, D. Credgington, D. Beljonne, R. H. Friend, and N. C. Greenham, J. Phys. Chem. Lett. **9**, 4053 (2018).

[46] K. Stavrou, A. Danos, T. Hama, T. Hatakeyama, and A. Monkman, ACS Appl. Mater. Interfaces **13**, 8643 (2021).

[47] V. V. Patil, H. L. Lee, I. Kim, K. H. Lee, W. J. Chung, J. Kim, S. Park, H. Choi, W.-J. Son, S. O. Jeon, and J. Y. Lee, Adv. Sci. **8**, 2101137 (2021).

[48] C. M. Marian, Wiley Interdiscip. Rev.: Comput. Mol. Sci. **2**, 187 (2012).

[49] J. Tatchen, N. Gilka, and C. M. Marian, Phys. Chem. Chem. Phys. **9**, 5209 (2007).

[50] H. Ågren, O. Vahtras, and B. Minaev, Adv. Quantum Chem. **27**, 71 (1996).

[51] T. Moitra, P. Karak, S. Chakraborty, K. Ruud, and S. Chakrabarti, Phys. Chem. Chem. Phys. **23**, 59 (2021).

[52] C. M. Marian, J. Phys. Chem. C **120**, 3715 (2016).

[53] P. Lundberg, Y. Tsuchiya, E. M. Lindh, S. Tang, C. Adachi, and L. Edman, Nat. Commun. **10**, 5307 (2019).

[54] R. Ianconescu and E. Pollak, J. Phys. Chem. A **108**, 7778 (2004).

[55] Q. Peng, Y. Yi, Z. Shuai, and J. Shao, J. Chem. Phys. **126**, 114302 (2007).

[56] B. de Souza, G. Farias, F. Neese, and R. Izsák, J. Chem. Theory Comput. **15**, 1896 (2019).

[57] Q. Peng, Y. Niu, Q. Shi, X. Gao, and Z. Shuai, J. Chem. Theory Comput. **9**, 1132 (2013).

[58] Q. Peng, Y. Niu, C. Deng, and Z. Shuai, Chem. Phys. **370**, 215 (2010).

[59] S. Banerjee, A. Baiardi, J. Bloino, and V. Barone, J. Chem. Theory Com-put. **12**, 774 (2016).

[60] R. Borrelli, A. Capobianco, and A. Peluso, J. Phys. Chem. A **116**, 9934 (2012).

[61] A. Baiardi, J. Bloino, and V. Barone, J. Chem. Theory Comput. **9**, 4097 (2013).

[62] Y. Niu, Q. Peng, and Z. Shuai, Sci. China, Ser. B: Chem. **51**, 1153 (2008).

[63] Y. Niu, Q. Peng, C. Deng, X. Gao, and Z. Shuai, J. Phys. Chem. A **114**, 7817 (2010).

[64] M. Etinski, J. Tatchen, and C. Marian, J. Chem. Phys. **134**, 154105 (2011).

[65] M. Etinski, V. Rai-Constapel, and C. Marian, J. Chem. Phys. **140**, 114104 (2014).

[66] P. Karak and S. Chakrabarti, Phys. Chem. Chem. Phys. **22**, 24399 (2020).

[67] B. de Souza, F. Neese, and R. Izsák, J. Chem. Phys. **148**, 034104 (2018).

[68] P. Karak, K. Ruud, and S. Chakrabarti, J. Phys. Chem. Lett. **12**, 9768 (2021).

[69] P.Karak and S.Chakrabarti, (2022), RISC rate constant program, Ver. 1.0. https://github.com/swapanchem/Rate-constant-RISC. DOI: 10.5281/zen-odo.6961475.

[70] A. C. Albrecht, J. Chem. Phys. **38**, 354 (1963).

[71] M. Frigo and S. Johnson, Proc. IEEE **93**, 216 (2005).

[72] Y. Zhao and D. G. Truhlar, Theor. Chem. Acc. **120**, 215 (2008).

[73] S. Miertuš, E. Scrocco, and J. Tomasi, Chem. Phys. **55**, 117 (1981).

[74] M. J. Frisch, G. W. Trucks, H. B. Schlegel, G. E. Scuseria, M. A. Robb, J. R. Cheeseman, G. Scalmani, V. Barone, G. A. Petersson, H. Nakatsuji, X. Li, M. Caricato, A. V. Marenich, J. Bloino, B. G. Janesko, R. Gom-perts, B. Mennucci, H. P. Hratchian, J. V. Ortiz, A. F. Izmaylov, J. L. Sonnenberg, D. Williams-Young, F. Ding, F. Lipparini, F. Egidi, J. Go-ings, B. Peng, A. Petrone, T. Henderson, D. Ranasinghe, V. G. Zakrzewski, J. Gao, N. Rega, G. Zheng, W. Liang, M. Hada, M. Ehara, K. Toyota, R. Fukuda, J. Hasegawa, M. Ishida, T. Nakajima, Y. Honda, O. Kitao, H. Nakai, T. Vreven, K. Throssell, J. A. Montgomery, Jr., J. E. Peralta, F. Ogliaro, M. J. Bearpark, J. J. Heyd, E. N. Brothers, K. N. Kudin, V. N. Staroverov, T. A. Keith, R. Kobayashi, J. Normand, K. Raghavachari, A. P. Rendell, J. C. Burant, S. S. Iyengar, J. Tomasi, M. Cossi, J. M. Millam, M. Klene, C. Adamo, R. Cammi, J. W. Ochterski, R. L. Martin, K. Mo-rokuma, O. Farkas, J. B. Foresman, and D. J. Fox, "Gaussian 16 Revision C.01," (2016), gaussian Inc. Wallingford CT.

[75] C. Adamo and V. Barone, J. Chem. Phys. **110**, 6158 (1999).

[76] T. Yanai, D. P. Tew, and N. C. Handy, Chem. Phys. Lett. **393**, 51 (2004).

[77] J.-D. Chai and M. Head-Gordon, Phys. Chem. Chem. Phys. **10**, 6615 (2008).

[78] F. Aquilante, J. Autschbach, A. Baiardi, S. Battaglia, V. A. Borin, L. F. Chibotaru, I. Conti, L. De Vico, M. Delcey, I. Fdez. Galván, N. Ferré, L. Freitag, M. Garavelli, X. Gong, S. Knecht, E. D. Larsson, R. Lindh, M. Lundberg, P. Å. Malmqvist, A. Nenov, J. Norell, M. Odelius, M. Olivucci, T. B. Pedersen, L. Pedraza-González, Q. M. Phung, K. Pierloot, M. Reiher, I. Schapiro, J. Segarra-Martí, F. Segatta, L. Seijo, S. Sen, D.-C. Sergentu, C. J. Stein, L. Ungur, M. Vacher, A. Valentini, and V. Veryazov, J. Chem. Phys. **152**, 214117 (2020).

[79] I. Fdez. Galván, M. Vacher, A. Alavi, C. Angeli, F. Aquilante, J. Autschbach, J. J. Bao, S. I. Bokarev, N. A. Bogdanov, R. K. Carlson, L. F. Chibotaru, J. Creutzberg, N. Dattani, M. G. Delcey, S. S. Dong, A. Dreuw, L. Freitag, L. M. Frutos, L. Gagliardi, F. Gendron, A. Giussani, L. González, G. Grell, M. Guo, C. E. Hoyer, M. Johansson, S. Keller, S. Knecht, G. Kovačević, E. Källman, G. Li Manni, M. Lundberg, Y. Ma, S. Mai, J. P. Malhado, P. Å. Malmqvist, P. Marquetand, S. A. Mewes, J. Norell, M. Olivucci, M. Oppel, Q. M. Phung, K. Pierloot, F. Plasser,

M. Reiher, A. M. Sand, I. Schapiro, P. Sharma, C. J. Stein, L. K. Søorensen, D. G. Truhlar, M. Ugandi, L. Ungur, A. Valentini, S. Vancoillie, V. Veryazov, O. Weser, T. A. Wesołowski, P.-O. Widmark, S. Wouters, A. Zech, J. P. Zobel, and R. Lindh, J. Chem. Theory Comput. **15**, 5925 (2019).

[80] F. Neese, Wiley Interdiscip. Rev. Comput. Mol. Sci. **2**, 73 (2012).

[81] F. Neese, Wiley Interdiscip. Rev. Comput. Mol. Sci. **8**, e1327 (2018).

[82] X. Gao, S. Bai, D. Fazzi, T. Niehaus, M. Barbatti, and W. Thiel, J. Chem. Theor. Comput. **13**, 515 (2017).

[83] I. Tavernelli, B. F. E. Curchod, A. Laktionov, and U. Rothlisberger, J. Chem. Phys. **133**, 194104 (2010).

[84] R. Send and F. Furche, J. Chem. Phys. **132**, 044107 (2010).

[85] S. Matsika, Chem. Rev. **121**, 9407 (2021).

[86] A. J. Gillett, A. Pershin, R. Pandya, S. Feldmann, A. J. Sneyd, A. M. Alvertis, E. W. Evans, T. H. Thomas, L.-S. Cui, B. H. Drummond, G. D. Scholes, Y. Olivier, A. Rao, Friend, R. H., and D. Beljonne, Nat. Mater. (2022), 10.1038/s41563-022-01321-2.

[87] M. A. El-Sayed, J. Chem. Phys. **38**, 2834 (1963).